Chalcogenide Letters Vol. 21, No. 10, October 2024, p. 819 - 828

Morphology and structural properties of $Sb_2(S_xSe_{1-x})_3$ thin film absorbers for solar cells

M. S. Tivanov [b,*], T. M Razykov [a], K.M Kuchkarov [a,b,*], A. N. Olimov [a], R. R. Khurramov [a], D. Z. Isakov [a], Z. A. Makhmudov [a], M. Pirimmetov [a], A. Nasirov [c], D. S. Bayko [b], O. V. Korolik [b]

[a]*Physics-Technical Institute, Academy of Sciences of the Republic of Uzbekistan, 100084, Tashkent, Chingiz Aitmatov Street, 2B*

[b]*Faculty of Physics, Belarusian State University Republic of Belarus, 220030 Minsk, Nezavisimosti Ave. 4*

[c]*National University of Uzbekistan named after Mirzo Ulugbek Uzbekistan, Tashkent, University str., 4*

Using the thermal evaporation method, thin crystalline films of $Sb_2(S_x\ Se_{1-x})_3$ are produced at the substrate temperature of 300°C. The mixed powders of the Sb_2S_3 and Sb_2Se_3 is used as a source material. The influence of the S/Se component ratio on the morphology and structural characteristics of $Sb_2(S_xSe_{1-x})_3$ thin films is investigated. As demonstrated by the results of X-ray energy dispersive spectroscopy, the formed films of $Sb_2(S_xSe_{1-x})_3$ have a components ratio close to the stoichiometry. Besides, Morphological and structural analyses reveal significant differences in the surface morphology of $Sb_2(S_xSe_{1-x})_3$ thin film absorbers, indicating that the properties of the films vary as a function of the S/Se composition ratio.

(Received July 24, 2024; Accepted October 18, 2024)

Keywords: Sb_2Se_3, Sb_2S_3, $Sb_2(S_xSe_{1-x})_3$ thin film absorber, Surface morphology, Crystalline structure

1. Introduction

In the global photovoltaic (PV) market, materials like Si, CdTe, and $Cu(In,Ga)Se_2$ are currently leading with efficiencies of 26.7%, 22.1% and 23.35%, respectively [1].

Despite their extensive utilization, these materials present significant challenges in the fabrication of photovoltaic (PV) modules. For instance, a major drawback of Si-based solar cells is that silicon possesses a suboptimal band gap of 1.1 eV and a relatively low absorption coefficient ($\sim 10^2$ cm^{-1}), necessitating the use of wafers with a thickness of 100–200 μm, which increases material costs [2]. Additionally, the large-scale implementation of thin-film solar cells based on $Cu(In,Ga)Se_2$ and CdTe is constrained by the limited natural availability of indium (In) and gallium (Ga), as well as the environmental toxicity associated with cadmium (Cd) [2].

Researchers have been carried out detailed investigations to the use of chalcogenide binary compounds such as Sb_2Se_3, Sb_2S_3, and their solid solutions $Sb_2(S_x,Se_{1-x})_3$ (chemical formula Sb_2X_3) as absorbing layers for solar cells [3,4]. This attention is due to their physical properties that closely resemble those of $Cu(In,Ga)(Se,S)_2$ including *p*-type conductivity, a bandgap (E_g) from 1.13 to 1.78 eV, a high absorption coefficient ($\alpha > 10^5 cm^{-1}$ in the visible region), low melting temperatures (Sb_2Se_3-612°C, Sb_2S_3-550°C), and high partial vapor pressure. Besides, chemical components in these materials have cost-effectiveness (abundant in nature) and stable under external influences [7]. This creates the prerequisites for the large-scale production of efficient solar cells on the basis of these elements.

Currently, $Sb_2(S_x,Se_{1-x})_3$ thin film solar cells show efficiency ranging from 5.6% to 10.75% [8-22]. This still relatively low efficiency in photoelectric conversion limits the industrial production of $Sb_2(S_xSe_{1-x})_3$ films based solar cells. However, the theoretical upper limit for the efficiency of solar cells on the base of $Sb_2(S_xSe_{1-x})_3$ films is approximately 32.88% according to Shockley-Quisser

* Corresponding authors: k.kuchkarov@mail.ru
https://doi.org/10.15251/CL.2024.2110.819

(SQ) limit [23]. Therefore, it is possible to increase their efficiency by controlling the structure, chemical and phase composition of the films.

Recently, we studied the morphological and structural characteristics of Sb_2Se_3 photovoltaic absorbers synthesized via chemical molecular beam deposition (CMBD) using pieces of the binary compound Sb_2Se_3 as a source material at different substrate temperatures. The results revealed that the films exhibited antimony enrichment and an orthorhombic crystal structure, with predominant orientations along the [120] and [221]; the crystal sizes of the Sb_xSe_y films, in rod-like formations, ranged between 0.5 and 8.0 μm [24,25].

This work presents the results of a study of the crystal structure and morphological properties of thin films of the $Sb_2(S_xSe_{1-x})_3$ solid solution fabricated via vacuum thermal evaporation on the dependence of the S/Se ratio.

2. Experimental details

Thin films of the $Sb_2(S_xSe_{1-x})_3$ are obtained by vacuum thermal evaporation method. Sb_2S_3 and Sb_2Se_3 powders with 99.999% semiconductor purity are used as the initial materials, with varying SbS/(SbS+SbSe) ratios ranging from 0 to 1. The process of powder evaporation is conducted using quartz evaporators (crucibles) prepared by annealing molybdenum cylindrical spirals 3-4 times under high vacuum conditions (10^{-5}-10^{-6} mmHg). The distance between the substrate and the crucibles within the working chamber measures 5 cm. Prior to the deposition process of $Sb_2(S_xSe_{1-x})_3$ thin films, the crucibles with evaporated materials were degassed. The deposition process for the thin film occurs under residual gas pressures of 10^{-5}-10^{-6} mmHg in a vacuum chamber.

During the $Sb_2(S_xSe_{1-x})_3$ crystal growth, the substrate temperature is maintained at 300°C, while the evaporator temperature during film deposition is approximately 600°C. The deposition rate of the films is approximately ~0.6 μm/min. After application, the films are cooled slowly under high vacuum conditions. The thickness of the deposited films is determined using an FA 120 4C balance (with an accuracy of 0.1 mg) and is approximately 2μm.

The elemental components of the obtained $Sb_2(S_xSe_{1-x})_3$ films was identified by means of X-ray spectral microanalysis (XMA) using an energy-dispersive nitrogen-free spectrometer Aztec Energy Advanced X-Max 80. Surface morphology features are examined with a LEO1455VP scanning electron microscope (SEM) equipped with secondary and reflected electron sensors. The surface topography is investigated using a SOLVER NANO atomic force microscope (AFM). Scanning is carried out in semi-contact mode with a probe with a tip radius of 10 nm at a resonant frequency of 178 kHz. High-resolution X-ray diffraction (XRD) patterns are obtained using a Rigaku Ultima IV diffractometer in the sliding beam geometry, data in the $2\theta = 10°–60°$ angle range with CuKα radiation (wavelength of 0.15418 nm). Raman spectra are measured at room temperature on a Nanofinder HE confocal spectrometer (LOTIS TII) with a solid-state laser emitting at a 532 nm wavelength. Laser radiation with a power of 60 μW was concentrated onto the sample surfaces within a circular area approximately 0.7 μm in diameter, with a signal accumulation time ranging from 30 to 60 seconds. The spectral resolution achieved was at least 2.5 cm^{-1}.

3. Result and discussion

The C content (at.%) of chemical elements in thin films, determined with energy-dispersive X-ray spectroscopy, is given in Table 1. From the table analysis, it is visible that the component ratio aligns well with stoichiometry. A typical energy spectrum of the synthesized thin films is shown in Fig. 1(a).

Table 1. Chemical composition of $Sb_2(S_xSe_{1-x})_3$ films.

Sample No.		**1**	**2**	**3**	**4**	**5**	**6**	**7**	**8**	**9**	**10**
C, at. %	Sb	40.22	40.38	40.53	39.9	39.81	39.76	39.93	39.45	38.92	40.76
	S	-	8.29	12.98	23.87	25.67	32.73	40.09	49.75	51.26	59.24
	Se	59.78	51.33	46.49	36.23	34.51	27.51	19.98	10.8	9.83	-
Sb/(S+Se)		0.67	0.68	0.68	0.66	0.66	0.66	0.66	0.65	0.64	0.69
x= S/(S+Se)		0.00	0.14	0.22	0.40	0.43	0.53	0.67	0.82	0.84	1.00

The multilayer maps illustrating the distribution of chemical elements on the film surfaces show a relatively regular spread of all components of the $Sb_2(S_xSe_{1-x})_3$ solid solution over the surface of the synthesized films (Fig. 1(b)).

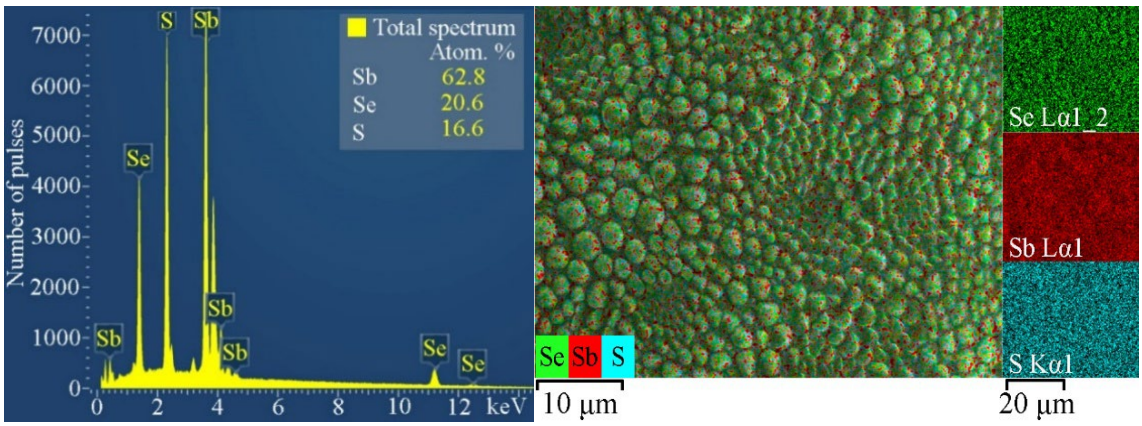

Fig. 1. (a) The energy spectrum of characteristic X-ray radiation of the $Sb_2(S_xSe_{1-x})_3$ film with a ratio S/(S+Se) = 0.67; (b) Map of the distribution of chemical elements on the surface of the $Sb_2(S_xSe_{1-x})_3$ film with a ratio S/(S+Se) = 0.67.

The surface morphology of $Sb_2(S_xSe_{1-x})_3$ films can be assessed through scanning electron micrographs (SEM) shown in Fig. 3. Based on SEM micrographs, it is evident that the microstructure (shape and size of crystallites) varies depending on the S/(S+Se) ratio of the films. Microcrystallites of the $Sb_2(S_xSe_{1-x})_3$ thin films consisting of different S/(S+Se) ratios show uniform distribution over the surface. As the S/(S+Se) ratio changes, the crystallite shapes change, and crystallite sizes increase with a higher proportion of S in the solid solution.

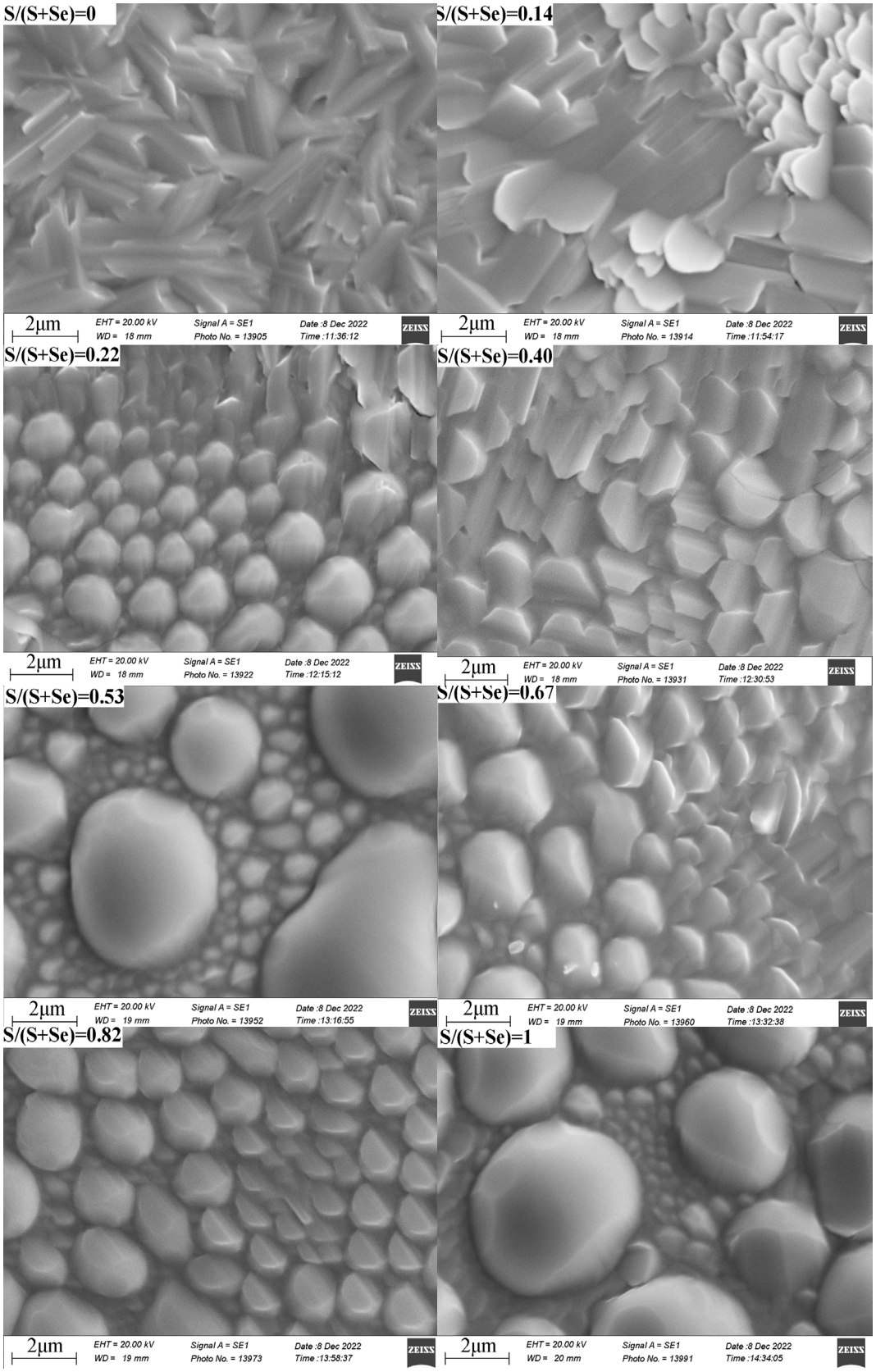

Fig. 3. The surface morphology of $Sb_2(S_xSe_{1-x})_3$ films assessed by scanning electron micrographs (SEM).

Samples with S/(S+Se) = 0 and S/(S+Se) = 0.14 have similar surface characteristics, significantly different from the other samples. The surface of the S/(S+Se) = 0 sample consists of

flat oblong crystallites that are close to a rectangle with sharp edges, measuring 2–3 μm by 0.5–0.8 μm. Likewise, the surface of the S/(S+Se) = 0.14 sample has similar crystallites, but with a greater size range: from small crystallites measuring 2 μm by 1 μm to larger crystallites measuring 3–6 μm by 1 μm. The S/(S+Se) = 0 sample has sharp, uneven edges, pointed towards the edge, while the S/(S+Se) = 0.14 sample has a rounded shape.

Samples with S/(S+Se) = 0.22 and S/(S+Se) = 0.40 have similar crystallites as the sample S/(S+Se) = 0.14, but in much smaller quantities. Instead, the majority of their surfaces have either large, rounded drop-shaped crystallites with diameters ranging from 0.25 μm to 3 μm in S/(S+Se) = 0.22 or sharp-edged crystallites similar to regular hexagons, measuring from 1.5 μm to 3 μm in S/(S+Se) = 0.40. Also, it should be noted that the surface of the sample S/(S+Se) = 0.40 differs from all others in the almost complete absence of crystallites smaller than 1.5 μm.

Other samples have similar surfaces and consist of almost perfectly round drop-shaped crystallites of various sizes. The smallest measurement of crystallite diameter that could be measured using micrographs in all samples from S/(S+Se) = 0.43 to S/(S+Se) = 1 is 0.25 μm. S/(S+Se) = 0.43 and S/(S+Se) = 0.84 samples are covered in the smallest drop-shaped crystallites, with diameters of not more than 2μm. S/(S+Se) = 0.53, S/(S+Se) = 0.67, S/(S+Se) = 0.82, and S/(S+Se) = 1 samples are practically indistinguishable, having crystallite sizes from 0.25 μm to 6 μm. The surface of the sample S/(S+Se) = 0.82 has crystallites with a maximum size of up to 6 μm. This indicates that with the increase in the sulfur fraction, the number of flat crystallites close in shape to a rectangle decreases, ultimately reaching an absence at S/(S+Se) = 0.43.

Studies conducted using AFM have shown a highly intricate surface relief in the films. Additionally, there is also a clear correlation between surface roughness and crystallite sizes: larger crystallites correspond to greater roughness. Figure 4 shows typical AFM images of surface regions of $Sb_2(S_xSe_{1-x})_3$ films with a size of 20×20 μm.

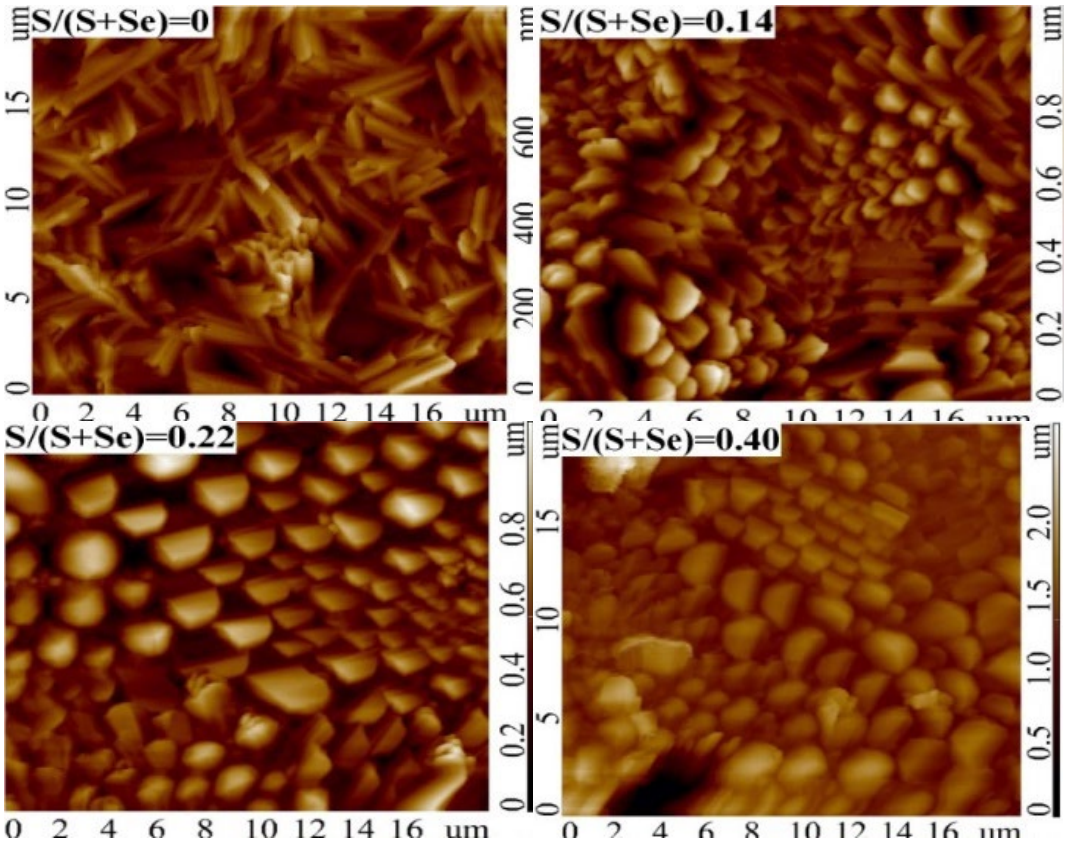

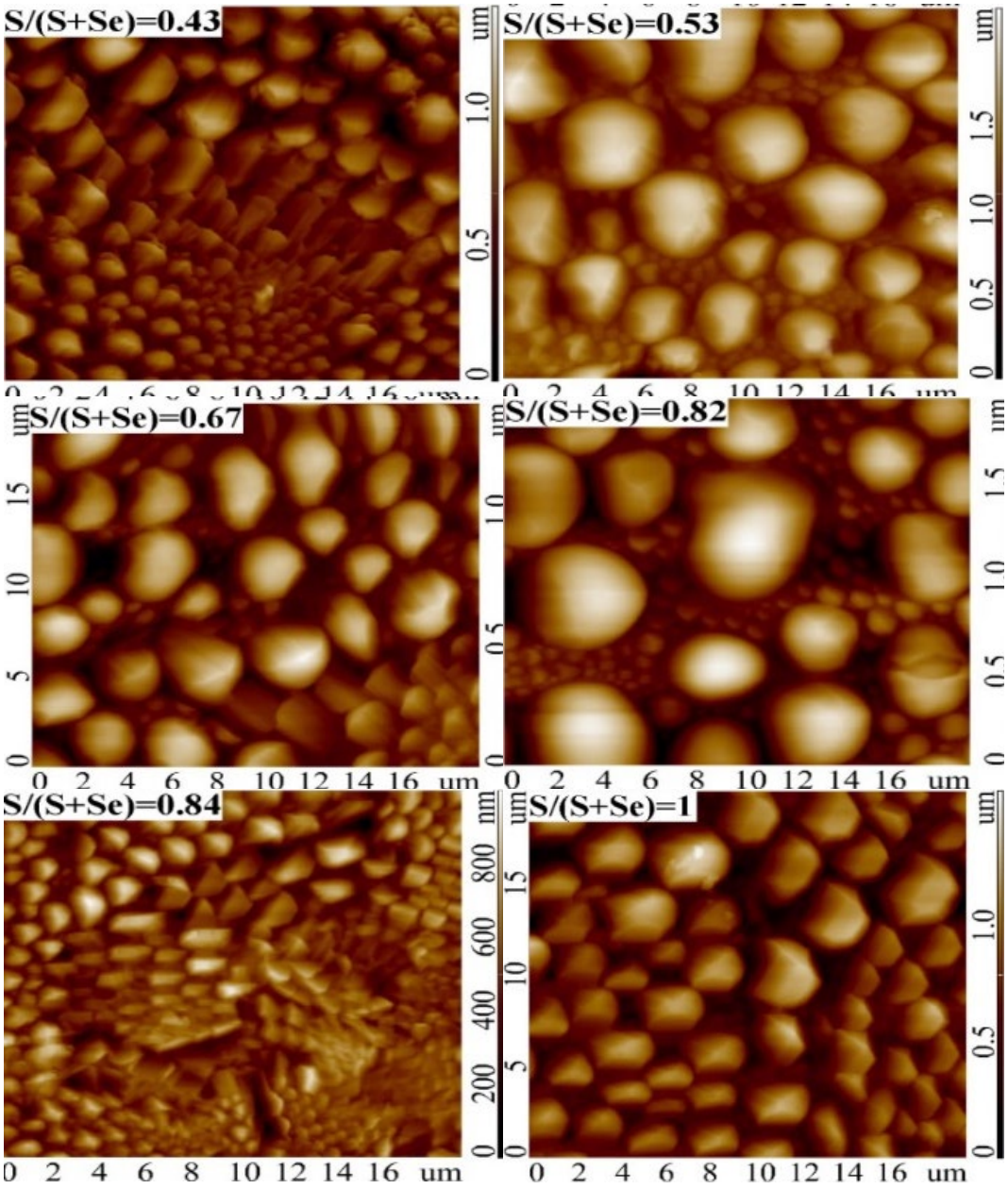

Fig. 4. AFM images of the surface of $Sb_2(S_xSe_{1-x})_3$thin films.

The calculated film surface roughness parameters are given in Table 2. The root-mean-square roughness varies in the range from 0.10 μm to 0.29 μm. Samples exhibiting S/(S+Se) ratios between 0 and 0.43 have almost the same root-mean-square roughness, but they have a significant difference in their asymmetry Ssk and kurtosis Ska.

Table 2. Surface roughness parameters of $Sb_2(S_xSe_{1-x})_3$ thin films.

S/(S+Se)	0	0.14	0.22	0.40	0.43	0.53	0.67	0.82	0.84	1
Average height h, μm	0.52	0.85	0.88	0.67	0.53	1.08	0.99	0.87	0.64	0.66
Average roughness S_a, μm	0.14	0.14	0.15	0.16	0.15	0.34	0.20	0.33	0.21	0.22
Root mean square roughness S_q, μm	0.10	0.11	0.12	0.13	0.11	0.29	0.16	0.28	0.17	0.18
Skewness, S_{sk}	0.91	0.09	0.37	0.34	0.41	0.35	0.46	0.19	0.40	0.40
Excess, S_{ka}	6.58	6.53	4.21	5.06	3.49	2.43	3.17	2.21	2.84	2.80

For example, the S/(S+Se) = 0 sample has the maximum asymmetry Ssk = 0.91 (a sufficiently large proportion of the surface lies below the average surface height). The maximum kurtosis value of this sample is Ska = 6.58, characterized by sharp, narrow, and elongated peaks. In contrast, the S/(S+Se) = 0.14 sample shows a lower asymmetry value (Ssk = 0.09), implying a more balanced distribution of peaks and valleys on the surface, while maintaining a relatively high kurtosis value (Ska = 6.53) indicative of narrow, elongated peaks. Furthermore, samples with S/(S+Se) ranging from 0.22 to 0.43 show decreased asymmetry (Ssk = 0.34÷0.41), signifying an increase in the proportion of the surface located above the midline of the relief. This suggests that the elevated parts of the relief are more substantial and have larger sizes. Other samples with S/(S+Se) > 0.43 are characterized by a plateau-kurtic surface with massive flat-topped peaks.

The structural analysis of deposited films of the $Sb_2(S_xSe_{1-x})_3$ films is conducted using XRD. Fig. 5 shows the XRD results of $Sb_2(S_xSe_{1-x})_3$ ($0<x<1$) films and the Sb_2Se_3 and Sb_2S_3 compounds. All films exhibit an orthorhombic structure with space group Pnma. From the XRD patterns given in Fig. 5, it is evident that as the ratio of the components S/(S+Se) increases, the intensity of the peaks (211) and (221) also increases, and the position shifts towards larger angles, 2θ. This phenomenon arises from the decrease in lattice parameters caused by the replacement of larger selenium atoms with smaller sulfur atoms.

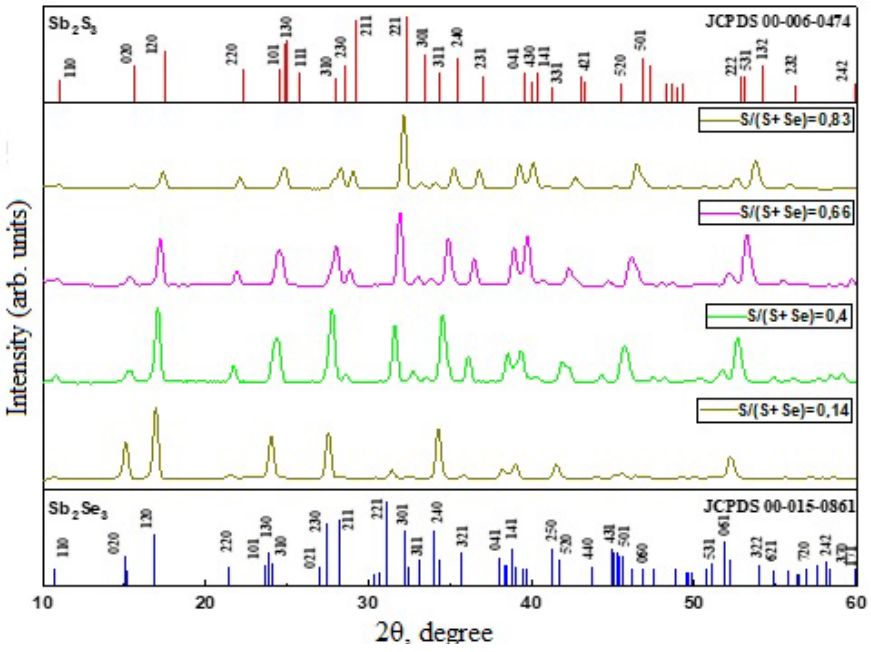

Fig. 5. X-ray diffraction patterns of synthesized $Sb_2(S_xSe_{1-x})_3$ films.

Two diffraction peaks at (211) and (221) indicate a crystal structure with a predominant crystallographic orientation (*hk*1), indicative of highly efficient charge carrier transport. This orientation is because of the special structure of $Sb_2S(e)_3$ crystals, consisting of ribbon-like units $(Sb_4S(e)_6)_n$, bound by weak Van der Waals forces through direction of the [010] and [100] [27-31].

Figure 6 shows the Raman spectra of $Sb_2(S_xSe_{1-x})_3$ thin films with different S/(S+Se) ratios. For $x = 0$, the Raman spectrum exhibits peaks characteristic of the Sb_2Se_3 compound: 80 cm^{-1}, a group of weakly resolved peaks in the range 100-135 cm^{-1}, as well as peaks ~151-153 $см^{-1}$, ~184-193 $см^{-1}$, ~210-211 $см^{-1}$ [32–34]. The Raman peak near 153 cm^{-1} corresponds to the A_{2u} vibration of the Sb-Sb bond, while those around 191 and 210 cm^{-1} are usually associated with the Ag mode of Sb-Se-Sb bending vibrations. Peaks in the region of small shifts (up to 130 cm^{-1}) are associated with vibrations of Se atoms [35-36].

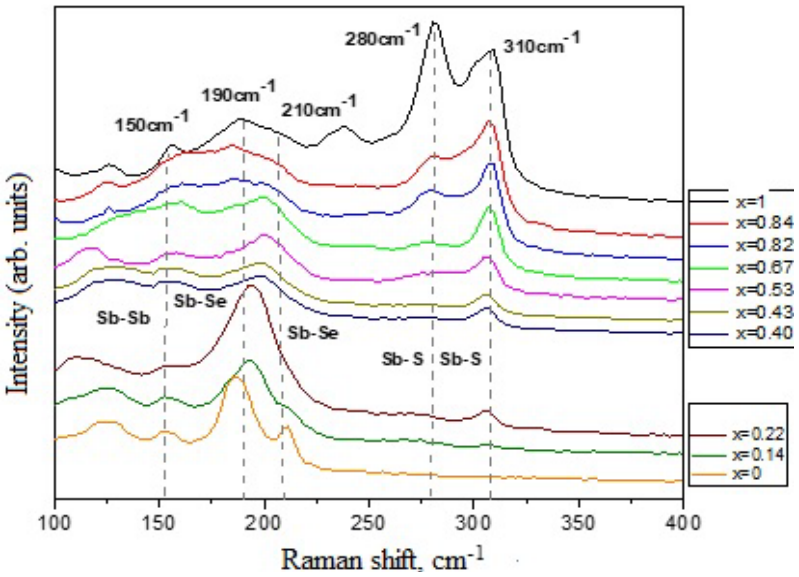

Fig. 6. Raman spectra of $Sb_2(S_xSe_{1-x})_3$ thin films.

As the ratio $x = S/(S+Se)$ increases, peaks associated with Sb_2S_3 start to appear in the Raman spectra. In the low-shift region (up to 220 cm^{-1}), Sb_2S_3 exhibits peaks that closely align with those of Sb_2Se_3 [32,37-40] since both compounds belong to the space group Pnma, and it makes their distinction impossible. However, Sb_2S_3 is distinguished by the existence of peaks at 241, 286, 308, and 314 cm^{-1} [37-38], some of which, in our case, are recorded already for $x = 0.14$. As the component ratio S/(S+Se) increases, the intensity of the peaks at 190 cm^{-1} and 210 cm^{-1} decreases, while the intensity of the peaks at 280 cm^{-1} and 310 cm^{-1} increases. Thus, for films with $0 < x < 1$, the presence of peaks indicative of both Sb_2Se_3 and Sb_2S_3 in the Raman spectra indirectly suggests the formation of $Sb_2(S_xSe_{1-x})_3$ solid solutions, which aligns with the results of *X*-ray diffraction analysis.

4. Conclusion

Thin films of $Sb_2(S_xSe_{1-x})_3$ solid solutions are obtained by vacuum deposition method.

Using energy-dispersive X-ray spectroscopy, it is determined that the resulting $Sb_2(S_xSe_{1-x})_3$ films have a Sb/(S+Se) component ratio close to stoichiometry, indicating a uniform distribution of all components (Sb, S, Se) across the surface of the synthesized thin films.

The scanning electron microscopy and X-ray diffraction analysis results revealed that all films possess an orthorhombic crystal structure, predominantly oriented along the [hk1] orientation, with crystallite sizes ranging from 0.25 to 6 μm. Additionally, increasing the S/(S+Se) atomic

concentration ratio results in a modification of crystallite morphology. An atomic force microscopy study of the films shows that the root mean square roughness increases with increasing S/(S+Se).

Raman spectroscopy data for thin films of $Sb_2(S_xSe_{1-x})_3$ indicate that with increasing component ratio S/(S+Se), the intensity of the peaks at 190 cm^{-1} and 210 cm^{-1} decreases, while the intensity of the peaks at 280 cm^{-1} and 310 cm^{-1} increases.

The results of the research can be used in future applications to obtain thin films of $Sb_2(S_xSe_{1-x})_3$ with specific compositions, morphology and structure, and help ensure maximum efficiency of solar cells based on them.

Acknowledgments

This work was supported by the Basic Research Program of the Academy of Sciences of the Republic of Uzbekistan, Ministry of innovative development of the Republic of Uzbekistan (Grant № FZ-2020102944) and the State Research Program of the Republic of Belarus “Material Science, New Materials and Technologies”.

References

[1] MA. Green, Ewan D. Dunlop, Jochen Hohl-Ebinger, Masahiro Yoshita, Nikos Kopidakis, Xiaojing Hao, Prog Photovolt Res Appl.2023; pp: 3-16. 629–638; https://doi.org/10.1002/pip.3646
[2] Razykov, T.M., Ferekides, C.S., et al., Sol. Energy, 2011, vol. 85, pp. 1580–1608; https://doi.org/10.1016/j.solener.2010.12.002
[3] Xiaomin Wang, Rongfeng Tang, Chunyan Wu, Journal of Energy Chemistry 27 (2018) 713–721; https://doi.org/10.1016/j.jechem.2017.09.031
[4] M.M. Nicolás-Marín, J.R. González-Castillo, O. Vigil-Galán, Maykel Coure, Journal of Physics D: Applied Physics 55 (2022) 303001; https://doi.org/10.1088/1361-6463/ac5f32
[5] Abdurashid Mavlonov, Takhir Razykov, Fazal Raziq, et al., Solar Energy Volume 201, 1 May 2020, Pages 227-246; https://doi.org/10.1016/j.solener.2020.03.009
[6] Y. Zhou, L. Wang, S. Chen, S. Qin, X. Liu, J. Chen, D. Xue, M. Luo, Y. Cao, Y. Cheng, E. H. Sargent, J. Tang, Nature Photonics, 9 (2015) 409–415; https://doi.org/10.1038/nphoton.2015.78
[7] B. Yang, S. Qin, D. Xue, Chao Chen, Yi-su He, D. Niu, H. Huang, J. Tang, Prog. Photovolt: Res. Appl. 25 (2016) 113-122; https://doi.org/10.1002/pip.2819
[8] Xiaobo Hu, Jiahua Tao, Rui Wang, Youyang Wang, Yanlin Pan, Guoen Weng, Xianjia Luo, Shaoqiang Chen, Ziqiang Zhu, Junhao Chu, Hidefumi Akiyama, Journal of Power Sources 493 (2021) 229737; https://doi.org/10.1016/j.jpowsour.2021.229737
[9] Xiaomin Wang, Rongfeng Tang, Chenhui Jiang, Weitao Lian, Huanxin Ju, Guoshun Jiang,Zhiqiang Li, Changfei Zhu, Tao Chen. Adv. Energy Mater. 2020, 2002341; https://doi.org/10.1002/aenm.202002341
[10] Mamta, Yogesh Singh, K.K. Maurya, et al., Solar Energy Materials & Solar Cells 230 (2021) 111223; https://doi.org/10.1002/aenm.202002341
[11] Y.H., Kim, Y.B., Jeong, M. et al., Solar Energy Materials and Solar Cells, 2017, 172, 11–17; https://doi.org/10.1016/j.solmat.2017.07.004
[12] Weihuang Wang, Xiaomin Wang, Guilin Chen, el at., Bulletin of Materials Science, 2004, 27 (2), 85–111; https://doi.org/10.1007/BF0270849
[13] Kulkarni, S. Arote, H. Pathan, et.al., Materials for Renewable and Sustainable Energy, 4 (2015) 1; https://doi.org/10.1007/s40243-015-0058-5
[14] Y. Zhou, M. Leng, Z. Xia, et.al., Advanced Energy Materials, 4 (2014) 1301846; https://doi.org/10.1002/aenm.201301846
[15] M.D. Khan, M. Aamir, M. Sohail et.al., Solar Energy 169 (2018) 526; https://doi.org/10.1016/j.solener.2018.05.026
[16] X. Liu, J. Chen, M. Luo, et al., ACS Applied Materials Interfaces 6 (2014) 10687; https://doi.org/10.1021/am502427s

[17] Mustafa, F.I., Gupta, S., Goyal, N., et al., Journal of Optoelectronics and Advanced Materials, 11(12), 2019.
[18] Wang, L., Li, D.-B., Li, K., Chen, et al., Nature Energy, 2017, 2 (4), 17046; https://doi.org/10.1038/nenergy.2017.46
[19] Liu, X., Xiao, X., Yang, Y., et al., Progress in Photovoltaics: Research and Applications, 2017, 25 (10), 861–870; https://doi.org/10.1002/pip.2900
[20] Liang, G.-X., Zhang, X.-H., Ma, H.-L., et al., Solar Energy Materials and Solar Cells, 2017, 160, 257–262; https://doi.org/10.1016/j.solmat.2016.10.042
[21] Hutter, O.S., Phillips, L.J., Yates, P.J., et al., 2018 IEEE 7th World Conference on Photovoltaic Energy Conversion (WCPEC) (A Joint Conference of 45th IEEE PVSC, 28th PVSEC & 34th EU PVSEC). IEEE, pp. 0027–0031
[22] Xinsheng Liu, Jie Chen, Miao Luo, Appl. Mater. Interfaces 2014, 6, 10687−10695; https://doi.org/10.1021/am502427s
[23] https://ru.qwe.wiki/wiki/Photovoltaics, https://ru.qwe.wiki/wiki/Photovoltaics#Efficiency
[24] T. M. Razykov, A. Kh. Shukurov, K. M. Kuchkarov, et al., Applied Solar Energy volume 55, pages 376- 379, 2019; https://doi.org/10.3103/S0003701X19060094
[25] T. M. Razykov, K. M. Kuchkarov, M. S. Tivanov, B. A. Ergashev, R. Khurramov, D. Z. Isakov, Applied Solar Energy, 2022, Vol. 58, No. 4, pp. 461–465; https://doi.org/10.3103/S0003701X22040132
[26] S. Lu, Y. Zhao, X. Wen, D. Xue, C. Chen, K. Li, R. Kondrotas, C. Wang, J. Tang, Sol. RRL 3 (2019) 1800280; https://doi.org/10.1002/solr.201800280
[27] D. Wang, C. Song, X. Fu, X. Li, Journal of Crystal Growth, 281 (2005) 611-615; https://doi.org/10.1016/j.jcrysgro.2005.04.064
[28] V.L. Deringer, R.P. Stoffel, M. Wuttig, R. Dronskowski, Chem Sci, 6 (2015) 5255-5262; https://doi.org/10.1039/C5SC00825E
[29] Y. Zhou, Y. Li, J. Luo, D. Li, X. Liu, C. Chen, H. Song, J. Ma, D.-J. Xue, B. Yang, J. Tang, , Applied Physics Letters, 111 (2017) 013901; https://doi.org/10.1063/1.4991539
[30] D.B. Li, X. Yin, C.R. Grice, L. Guan, Z. Song, C. Wang, C. Chen, K. Li, A.J. Cimaroli, R.A. Awni, D. Zhao, H. Song, W. Tang, Y. Yan, J. Tang, Nano Energy, 49 (2018) 346-353; https://doi.org/10.1016/j.nanoen.2018.04.044
[31] Y. Zhou, L. Wang, S. Chen, S. Qin, X. Liu, J. Chen, D.J. Xue, M. Luo, Y. Cao, Y. Cheng, E.H. Sargent, J. Tang, Nature Photonics, 9 (2015) 409-415; https://doi.org/10.1038/nphoton.2015.78
[32] M.D. Khan, S.U. Awan, C. Zequine, C. Zhang, R.K. Gupta, N. Revaprasadu, ACS Applied Energy Materials 3(2), (2020) 1448. 1460; https://doi.org/10.1021/acsaem.9b01895
[33] P. Vidal-Fuentes, M. Guc, X. Alcobe, T. Jawhari, M. Placidi, A. Pérez-Rodríguez, E. Saucedo, V. Izquierdo Roca, 2D Mater., 6 (2019) 045054; https://doi.org/10.1088/2053-1583/ab4029
[34] A. Kumar, V. Kumar, A. Romeo, C. Wiemer, and G. Mariotto, J. Phys. Chem.C, 125 (36) (2021) 19858–19865; https://doi.org/10.1021/acs.jpcc.1c05047
[35] Z.G. Ivanova, E. Cernoskova, V.S. Vassilev, S.V. Boycheva, Materials Letters, 57 (2003) 1025 – 1028; https://doi.org/10.1016/S0167-577X(02)00710-3
[36] K. Nagata, K. Ishibashi, Ya. Miyamoto, Japanese Journal of Applied Physics, 20(3) (1981) 463 – 469; https://doi.org/10.1143/JJAP.20.463
[37] Y.A. Sorb, V. Rajaji, P.S. Malavi, U. Subbarao, P. Halappa, S.C. Peter, S. Karmakar and C. Narayana, J. Phys.: Condens. Matter, 28 (2016) 015602; https://doi.org/10.1088/0953-8984/28/1/015602
[38] P. Sereni, M. Musso, P. Knoll, P. Blaha, K. Schwarz, G. Schmidt, AIP Conf. Proc., 1267 (2010) 1131 – 1132; https://doi.org/10.1063/1.3482339
[39] Y, Liu, K.T.E. Chua, T.C. Sum, C.K. Gan, Phys. Chem. Chem. Phys. 16(1), 345–350 (2014). https://doi.org/10.1039/C3CP53879F
[40] C.J. Diliegros-Godines, J.S. Cruz, N.R. Mathews, M. Pal, J Mater Sci 53(16), 11562–11573 (2018); https://doi.org/10.1007/s10853-018-2420-3